Star Formation in the Northern Cloud Complex of NGC 2264

Abigail S. Hedden, Christopher K. Walker, and Christopher E. Groppi

Steward Observatory, University of Arizona, Tucson, AZ 85721

ahedden@as.arizona.edu

Harold M. Butner

Joint Astronomy Centre, Hilo, HI 96720

ABSTRACT

We have made continuum and spectral line observations of several outflow sources in the Mon OB1 dark cloud (NGC 2264) using the Heinrich Hertz Telescope (HHT) and ARO 12m millimeter-wave telescope. This study explores the kinematics and outflow energetics of the young stellar systems observed and assesses the impact star formation is having on the surrounding cloud environment. Our data set incorporates $^{12}CO\,(3-2)$, $^{13}CO\,(3-2)$, and $^{12}CO\,(1-0)$ observations of outflows associated with the sources IRAS 06382+1017 and IRAS 06381+1039, known as IRAS 25 and 27, respectively, in the northern cloud complex. Complementary $870\,\mu m$ continuum maps were made with the HHT 19 channel bolometer array. Our results indicate there is a weak $\leq\,0.5\,\%$ coupling between outflow kinetic energy and turbulent energy of the cloud. An analysis of the energy balance in the IRAS 25 and 27 cores suggests they are maintaining their dynamical integrity except where outflowing material directly interacts with the core, such as along the outflow axes.

Subject headings: stars: formation, ISM: individual - Mon OB1 (NGC 2264) - Clouds - ISM: jets and outflows - ISM: kinematics and dynamics - ISM: molecules - radio lines: ISM

1. Introduction

The Mon OB1 dark cloud lies toward the galactic anticenter and has been the subject of several large-scale molecular line surveys (Blitz 1979), (Oliver, Masheder, & Thaddeus 1996). Due to its location, there is little source confusion from intervening foreground and

background clouds. The relative proximity of this complex, 800 pc according to the work of Walker (1956), has also contributed to its survey appeal. The region of Mon OB1 associated with NGC 2264 has itself been the subject of several studies, including an unbiased ^{12}CO $(1-0)$ survey and the discovery of nine molecular outflows (Margulis & Lada 1985), (Margulis, Lada, & Snell 1988). Margulis, Lada, & Young (1989) presented the results of an IRAS survey of 30 discrete far-infrared sources, including IRAS 25 and IRAS 27. The IRAS Point Source Catalog (PSC) identifies IRAS 25 and IRAS 27 with objects IRAS 06382+1017 and IRAS 06381+1039, respectively. A systematic search for dense gas with CS observations revealed that these objects were associated with a $\sim 500 - 700$ M$_\odot$ clump (Wolf-Chase, Walker, & Lada 1995).

Wolf-Chase et al. (2003) used HIRES processing of IRAS data, ^{12}CO $(2-1)$ observations, and SCUBA continuum images to identify individual cores embedded within NGC 2264 and concluded that IRAS 25 and IRAS 27, initially thought to be Class I protostellar objects (Margulis, Lada, & Young 1989), consist of multiple sources in different evolutionary stages. They also find evidence for multiple outflow driving sources in the ^{12}CO$(2-1)$ data. In a wide field imaging survey of the NGC 2264 region of Mon OB1 in the infrared, H$_\alpha$, and ^{12}CO $(3-2)$, Reipurth et al. (2004) report several new Herbig-Haro (HH) objects near the star forming cores found by Wolf-Chase et al. (2003) and attempt to pinpoint their origins.

A primary goal of this work is to determine physical characteristics and outflow properties of IRAS 25 and 27. With this information, we hope to gain a better understanding of the star formation history, dynamics, and impact that these protostellar objects have on the surrounding cloud environment. In Section (2.), we describe the observations presented in this work. Section (3.) addresses the results of the continuum and spectral line observations of each of the sources, IRAS 25 and 27. In Section (4.), we discuss velocity centroid studies of the molecular line data and draw energetics comparisons to assess the impact star formation is having upon the cloud complex. A summary of our findings is presented in (5.)

2. Observations

2.1. Continuum mapping with the HHT

The continuum data presented in this work were obtained with the facility 19 channel array operating at the HHT on Mt. Graham, Arizona. This array, developed by E. Kreysa and collaborators, contains 19 individual broadband bolometric detectors sensitive around a central wavelength of $\lambda = 870\,\mu$m (345 GHz) and arranged in two concentric hexagonal rings surrounding a central pixel. The field of view of the array is $\sim 200''$ in diameter. Observations

were made during 2003 January $12 - 14^{th}$ and May $6 - 8^{th}$, and 2004 April $21 - 22^{nd}$ using On The Fly (OTF) mapping. With this technique, fully sampled $450'' \times 300''$ maps were made surrounding the sources IRAS 25 and 27 in NGC 2264. A total of six maps of IRAS 27 and three maps of IRAS 25 were combined to produce the data sets presented here. During observations, the pointing was checked each hour by observing a planet, such as Venus, Saturn, and Jupiter. For all of the data, the pointing varied by less than $4''$. These maps were corrected for the effects of atmospheric opacity using "skydip" scans taken prior to beginning and upon completion of each map. This correction is accomplished by fitting a polynomial function to the optical depth, at $870\,\mu$m as a function of elevation. The bolometer data were flux calibrated with images of Mars, Saturn, and the known submillimeter secondary calibrator source IRAS 16293-2422 (Sandell 1994) taken using a continuum on/off sequence technique. We estimate the flux calibration to be accurate within the $\sim 20\%$ level.

2.2. Spectral line observations

2.2.1. HHT data

In February and May of 2004, we obtained ^{12}CO $(3 - 2)$ and ^{13}CO $(3 - 2)$ spectral line data with the HHT toward known outflow regions, NGC 2264 O and NGC 2264 H, associated with IRAS 25 and 27, respectively. A summary of important observational parameters for these data is presented in Table 1. A set of $300'' \times 300''$ ^{12}CO $(3 - 2)$ fully sampled OTF maps were made surrounding the two IRAS sources. The pointing was monitored similar to the continuum observations and varied $< 5''$. A total of two separate maps, each with two polarization data, were made for NGC 2264 O & H. After careful calibration, maps were combined to produce the data described in Table 1. In addition, ^{13}CO $(3 - 2)$ Absolute Position Switched (APS) spectra were taken toward the locations of the IRAS sources as published in Margulis, Lada, & Young (1989). A total integration time of 140 s was spent on source for each APS ^{13}CO observation. The 2σ RMS of all observations has been included in Table 1.

The HHT facility dual-polarization, double-sideband 345 GHz receiver was used with two Acousto-Optical Spectrometer backends, each possessing 1 GHz total bandwidth and 2048 channels. Individual APS spectra were taken toward the positions of IRAS 25 and 27 at the beginning of each observing session and used to cross calibrate data sets taken on different days. Orion A ($\alpha_{1950} = 05^h\,32^m\,47.0^s$, $\delta_{1950} = -05°\,24'\,21''$) was used to calibrate the dual polarization data before they were combined. For ease of comparing data sets from different telescopes, the main beam efficiency (η_{mb}) of the 345 GHz receiver was measured and used to convert antenna temperature corrected for atmospheric extinction, T_A^*, to a main beam

brightness temperature, T_{mb}, according to $T_{mb} = T_A^*/\eta_{mb}$. Measurements of Saturn were used to find η_{mb} using Equation 1, where $T_R(planet)$ is the planet's brightness temperature, D is the angular diameter of the planet when it was observed, and θ is the telescope beam size. Measurements of Saturn made during observations resulted in η_{mb} values that varied $\sim 20\%$. Based on this variation, we adopt a value of $\eta_{mb} \approx 60\%$ for the 345 GHz receiver during this time.

$$\eta_{mb} = \frac{T_A^*(planet)}{T_R(planet)}[1 - exp(\frac{-D^2}{\theta^2}ln2)]^{-1} \tag{1}$$

2.2.2. 12m data

APS ^{12}CO $(1-0)$ observations of IRAS 25 and 27 were made at the ARO 12m millimeter-wave telescope near Tucson, AZ during April 2002. A summary of the observational information is presented in Table 1. A total integration time of 120 s was spent on source for each observation and 2σ RMS values are listed in Table 1. The 12m dual-polarization, single-sideband $90 - 116$ GHz receiver and Millimeter Autocorrelator (MAC) backend with 300 kHz total useable bandwidth and 8192 channels were used. Similar to the HHT data, both polarizations were combined in order to improve the signal-to-noise using Orion A as a cross-calibrator. The 12m makes measurements in terms of T_R^*, the observed antenna temperature corrected for atmospheric attenuation, radiative loss, and rearward scattering and spillover. In order to make meaningful comparisons between data sets, these measurements were converted to a T_{mb} scale using a procedure documented in Appendix C of the 12m manual. According to the manual, $T_{mb} = T_R^*/1.08$ for the $90 - 116$ GHz receiver at 115 GHz. With this conversion, the 12m data were compared with HHT spectra after the data sets were convolved to the same beam size. Measurements of T_{mb} for the 12m data are accurate to within $\sim 20\%$.

3. Results

3.1. Continuum Analysis

Results of the 870 μm HHT continuum data analysis are presented for IRAS 25 & 27. Table 2 lists the fluxes found at the positions of sources IRAS 25 & 27 and the associated continuum cores. The cores, labeled with S1, S2, and S3 extensions, were initially identified as emission peaks in 850 μm and 450 μm SCUBA maps (Wolf-Chase et al. 2003). We derived

$870\,\mu$m peak fluxes within multiple apertures for each of the sources, including $45''$ (for easy comparison with Wolf-Chase et al. (2003)) and $3'\times5'$, the size of the IRAS error ellipse at $100\,\mu$m.

Combining our $870\,\mu$m continuum data with bolometric observations of other observers and IRAS, we construct FIR SEDs (see Figure 1) for dust cores with $870\,\mu$m fluxes presented in Table 2. When IRAS data were used, the fluxes were taken from the PSC. At $60\,\mu$m & $100\,\mu$m, the IRAS the beam sizes are larger than the IRAS 25 source, indicating fluxes of the entire clump emission were found. When constructing the IRAS 25 FIR SED, measurements of the $870\,\mu$m emission of the whole clump were used. In order to incorporate SCUBA $450\,\mu$m & $850\,\mu$m data, we estimated the total flux found at these wavelengths by summing published fluxes within $45''$ apertures of the 25 S1 and S2 cores. For IRAS 27, $60\,\mu$m & $100\,\mu$m IRAS fluxes were incorporated in the FIR SED with the $870\,\mu$m fluxes measured within $45''$ apertures around the continuum cores IRAS 27 (27 S1), S2, and S3. Published SCUBA $450\,\mu$m & $850\,\mu$m measurements made within the same $45''$ apertures were included. When available (for sources 27 S1 & S2) $1300\,\mu$m fluxes were incorporated. A summary of continuum measurements for each source at all wavelengths where data are available is in Table 3 along with associated references.

In order to probe physical conditions of the continuum cores, FIR SEDs were fit with expressions of the following form (Hildebrand 1983):

$$F_\nu = \Omega_s B_\nu(T)(1 - e^{\tau_\nu}) \tag{2}$$

where Ω_s is the source size and

$$B_\nu(T) = \frac{2h\nu^3/c^2}{(e^{h\nu/kT} - 1)} \quad \& \quad \tau_\nu = (\nu/\nu_o)^\beta \tag{3}$$

In Equation 3, $B_\nu(T)$ is the Planck function, τ_ν describes the frequency dependent optical depth, β is the spectral index governing dust grain emissivity properties, and ν_o is the frequency where $\tau_\nu = 1$.

The results of fitting flux values to Equations 2 and 3 are illustrated in Figure 1 and Table 4 summarizes the details numerically. We have only attempted to fit the cold dust component ($\lambda \geq 60\,\mu$m) of the continuum emission that is responsible for the majority of the flux at mm and submm wavelengths. In all cases, except for IRAS 25, each continuum core was well fit by a single temperature blackbody (BB), similar to Equation 3. In order to obtain a good least-squares fit to each of these dust cores (IRAS 27 (27 S1), 27 S2, and 27 S3), source size (Ω_s), temperature (T), and spectral index (β) parameters were varied iteratively until a best fit solution was found.

Fitting SED curves to IRAS 25 flux measurements proved more complex, and a two temperature component BB function was used. In order to obtain a good, physically plausible fit to these data, both dust temperature components, T, and β indices were selected and held constant while the source sizes, Ω_s, were iteratively fit. The goodness of fit did not strongly depend upon the values of β chosen for the two components and therefore the resulting fit does not reflect unique or precise values of spectral index. Since spectral index is probably constant within the same molecular cloud complex, our choice of β used to fit the IRAS 25 emission was guided by solutions from iterative fits of IRAS 27 (27 S1), 27 S2, and 27 S3 SEDs. The temperatures of the two components fit to IRAS 25, 10 K and 40 K, were selected to be similar to the ~ 30 K obtained from using Wien's displacement law to estimate the characteristic dust temperature for IRAS 25. The two component BB fit was found to be rather sensitive to the values of temperature chosen. Based upon this sensitivity, the temperatures of the components are probably accurate to within 5K.

Luminosities (L_{FIR}) of continuum cores were found using $L_{FIR} = 3.1 \times 10^{-10} D^2 \int F_\nu d\nu$ (Walker, Adams, & Lada 1990) where L_{FIR} is in L$_\odot$, D is in pc, F_ν is in Jy, and ν is in GHz. Dust filling factors, $f_d = \Omega_s/\Omega_m$, were estimated by comparing values of Ω_s derived from the SEDs to half-power 870 μm source sizes, Ω_m. Table 4 presents the results of the FIR SED model fits and parameters for each of the cores examined. Using techniques similar to Hildebrand (1983), physical properties of the dust cores, including dust optical depth at 870 μm ($\tau_\nu = \tau_{870}$), column density (N_{H_2}), and total gas mass (M_{H_2}) were derived. Number density values (n_{H_2}) were found using the relation $M_{H_2}/(4/3\,\pi\,R^3\,m_{H_2})$ where m_{H_2} is the mass of a hydrogen molecule and R is the radius over which M_{H_2} was found. The visual extinction was estimated using the relation $A_v = 1.1 \times 10^{-21} N_{H_2}$ (Bohlin, Savage, & Drake 1978). The results of this analysis are presented in Table 5. In making these computations, we assumed a gas to dust ratio of 100 in mass, a grain density of $\rho = 3$ g cm^{-3}, and a dust particle radius of $a = 0.1\,\mu$m. These values are consistent with those determined by Hildebrand and are commonly used for molecular clouds in the galaxy.

At 870 μm, Figure 1 shows that the majority of the flux observed for IRAS 25 is due to the colder 10 K BB component. It is reasonable to obtain an upper limit to the amount of mass in the IRAS 25 core region by assuming that all flux at these wavelengths is attributable to the cold gas. Using the analysis tools described above, a limit of 140 M$_\odot$ was obtained for the IRAS 25 core (Table 5). Although this mass limit is large compared with the IRAS 27 core, it is not unexpected. The observed flux at 870 μm for IRAS 27 (Figure 1) is well described by a 30 K BB source and is weaker by about a factor of two when compared with IRAS 25 870 μm fluxes (Table 3). At these wavelengths, we observe comparatively more flux from a colder source, implying larger column density and core mass values for IRAS 25.

3.2. Spectral Line Observations

In this section, the results of ^{12}CO $(3-2)$ & ^{13}CO $(3-2)$ analyses are presented for IRAS 25 & 27. The CO$(3-2)$ spectra for both objects are single peaked features and possess broad line wings (~ 40 km s^{-1} in extent for IRAS 25 and ~ 50 km s^{-1} for IRAS 27). In order to investigate the spatial distribution of the outflow molecular gas, emission line wings were defined by comparing the ^{12}CO $(3-2)$ & ^{13}CO $(3-2)$ spectra (see Figure 2) and then used to make contour maps. The ^{13}CO $(3-2)$ line wings set the maximum extent of low velocity emission associated with the outflows. High velocity wings extended to where the ^{12}CO $(3-2)$ emission merged with the noise. Figure 2 illustrates these regions, including the line core, low, and high velocity wings for both IRAS 25 and 27 and Table 6 summarizes this information. In this table, the spectral line emission of the entire (full) red and blue wings (F RW & F BW) has been divided into low and high velocity (LV & HV) regions.

3.2.1. IRAS 25 (IRAS 06382+1017)

Contour maps of F RW and F BW integrated intensity were constructed for IRAS 25 using $I_{F\ RW} = \int_{8.8\ km\,s^{-1}}^{27.5\ km\,s^{-1}} T_A^*\ ^{12}dv$ & $I_{F\ BW} = \int_{-10.5\ km\,s^{-1}}^{5.6\ km\,s^{-1}} T_A^*\ ^{12}dv$, respectively. Figure 3 shows red (thin, solid contours) and blue wing (thin, dashed lines) ^{12}CO $(3-2)$ emission associated with outflow NGC 2264 O surrounding IRAS 25. Contours are superimposed on an $870\,\mu$m continuum OTF map (see Section (3.1)) and the figure includes locations of other sources discovered within the same region. Figure 3 shows two prominent blue outflow lobes, SEB & WB, and an elongated red emission lobe. Although a single red outflow lobe is detected, observations indicate that the emission is unresolved and two separate red lobes, ER & NWR, exist. Figure 4 is a contour map of the high velocity (HV) red and blue ^{12}CO $(3-2)$ emission associated with NGC 2264 O. A large fraction of the eastern red emission (ER) disappeared for the high velocity gas, leaving a clear view of the compact northwestern red (NWR) emission. This indicates that the ER and NWR emission possess different velocity components and suggests that the emission belongs to two different outflow lobes.

Our data support the existence of two ^{12}CO $(3-2)$ outflows in the region. Figure 4 aided in determining the orientations of the two outflows associated with NGC 2264 O. The high velocity gas traces an outflow oriented southeast (SEB) to northwest (NWR). The WB lobe and a portion of ER emission do not appear in this figure. This indicates these lobes have similar velocities and suggests they describe a second outflow. The existence of multiple molecular outflows within this region has been suggested by other authors (Piché, Howard, & Pipher 1995), (Wolf-Chase et al. 2003). Our observations of two ^{12}CO $(3-2)$ outflows fit

well with the work of Reipurth et al. (2004) and lend support to observations of recurring outflow activity taking place in the region surrounding IRAS 25 (Ogura (1995), Wolf-Chase et al. (2003), Reipurth et al. (2004)).

For clarity, the information contained in Figure 3 is summerized in the model sketch of the IRAS 25 region shown in Figure 5. The location of IRAS 25 is denoted with a box, and continuum peaks 25 S1 & 25 S2 associated with $850\,\mu$m & $450\,\mu$m SCUBA emission are shown with "X" symbols. IRAS 25 has been identified as the driving source for a large scale (0.48 pc) Herbig-Haro flow, HH 124 (Walsh, Ogura, & Reipurth 1992). Six knots of emission were observed (asterisks) and lie along the WB−ER outflow axis. This region also includes an IR reflection nebula (thick, gray contour in Figure 5) associated with IRAS 06382+1017 (Piché, Howard, & Pipher 1995) and two VLA sources (triangles) within the IRAS error ellipse (Rodríguez & Reipurth 1998).

In this complex environment, it is difficult to determine sources of the ^{12}CO $(3-2)$ outflows. Our observations and the work of Reipurth et al. (2004) indicate that the WB−ER outflow axis is well aligned with HH 124, suggesting that the IRAS object may be the source of this outflow emission. The axis of the SEB−NWR outflow is in proximity to many objects, including IRAS 25 and the submillimeter continuum sources. The source of this molecular outflow has not been determined (Reipurth et al. 2004), although it is oriented along the opening angle of the IR reflection nebula associated with IRAS 25 (see Figure 5). It is possible that two ^{12}CO $(3-2)$ molecular outflows emanate from IRAS 25; the WB−ER flow oriented along HH 124, and a SEB−NWR outflow along the IR reflection nebula opening angle.

The SEB−NWR outflow axis does not intersect well with IRAS 25. If the IRAS object is the source of the flow, this may imply that the outflow is redirected as it encounters dense ambient material. Figure 3 shows that the IRAS source is located near the edge of a dense, extended $870\,\mu$m continuum core. We estimate how dense this material would have to be in order to redirect the outflow and make comparisons with the results of the continuum analysis (n_{H_2} in Table 5). To redirect the flow, the clump pressure, given by the ideal gas law ($n_{cl}\,k\,T$) in LTE, must exceed the pressure of the outflowing material, $\dot{P}_{OF}/(\pi\,R^2)$. For an order of magnitude estimate, it is assumed the outflow acts mostly over an area encompassing its $1/2$ power contours. In this analysis, k is Boltzmann's constant, $T = 10$ K is the core temperature derived from continuum observations (see Table 4), $\dot{P}_{OF}$ is the outflow momentum rate (see Section (3.2.3)), and R is the average radius of $1/2$ power outflow contours. The minimum core density capable of redirecting the outflow is $n_{cl} \sim 10^7$ cm^{-3}. This is large compared with n_{H_2} (see Table 5), suggesting the density of the core is most likely not sufficient to influence outflows in the region.

It was suggested that IRAS 25 is a barely resolved binary system with a possible component ~ 1400 AU ($1.8''$ at the assumed distance of NGC 2264) from the primary at a position angle of $\sim 155°$ (Piché, Howard, & Pipher 1995). The presence of two outflows is consistant with IRAS 25 being a binary system and may explain the unusual morphology. The $870\,\mu$m continuum emission (Section (3.1)) can be used to estimate the mass of stellar objects in the system. Assuming that the bolometric luminosity (L_{FIR}) of this object (see Table 4) equals the accretion luminosity ($L_{acc} = GM\dot{M}_{acc}/R$), an upper limit to the mass of the central object is obtained. We assumed a typical radius of $R = 2 \times 10^{11}$ cm, ~ 3 R$_\odot$, for the hydrostatic core of an accreting protostellar object (Stahler, Shu, & Taam 1980) and the mass infall rate of an isothermal cloud, $\dot{M}_{acc} = 0.975\,c_s^3/G$ (Shu 1977), where $c_s = \sqrt{kT/m_{H_2}}$ is the cloud sound speed. Since material is accreted from a reservoir in close proximity to the protostar, the warmer continuum component $T = 40$ K (see Table 4) was used to calculate c_s. This simple analysis estimates $0.5\,$M$_\odot$ for the stellar object(s) associated with IRAS 25.

3.2.2. IRAS 27 (IRAS 06381+1039)

Similar to (Section (3.2.1)), ^{12}CO$\,(3-2)$ line wing integrated intensities were found for NGC 2264 H outflows surrounding IRAS 27 using $I_{F\ RW} = \int_{9.8\ km\,s^{-1}}^{28.5\ km\,s^{-1}} T_A^*\,^{12}dv$ & $I_{F\ BW} = \int_{-20.0\ km\,s^{-1}}^{6.7\ km\,s^{-1}} T_A^*\,^{12}dv$. Figure 3 shows the outflow emission (F RW = solid, thin lines and F BW = thin, dashed contours) superimposed on a map of $870\,\mu$m continuum emission. Other sources in the region are shown, including the location of the IRAS source (box) and 870 & $450\,\mu$m SCUBA emission peaks, 27 S1, 27 S2, & 27 S3. Our observations indicate there is evidence for two ^{12}CO$\,(3-2)$ outflows located near IRAS 27, supporting the recent work of Reipurth et al. (2004). Figure 4 shows the high velocity outflow emission that was used to help determine outflow orientations. The figure indicates HV gas traces an outflow oriented southeast (SER) to northwest (NWB). The northeastern (NEB) and southwestern (SWR) lobes vanish in Figure 4 indicating that they have similar velocities and describe a second outflow.

Figure 5 is a model sketch of the IRAS 27 system, showing the orientations of the ^{12}CO$\,(3-2)$ outflows. H$_2$, Hα, and [SII] images of the region reveal an IR source surrounded by a reflection nebula (thick, gray contour) and two giant HH outflows, HH 576 and 577 emanating from a core containing IRAS 27 (Reipurth et al. 2004). Figures 3 and 5 show submillimeter cores located along a dense ridge of $870\,\mu$m emission with molecular outflows oriented at large angles (nearly perpendicular) to the continuum ridge. It is difficult to determine the source of the ^{12}CO$\,(3-2)$ outflows, given their proximity to the continuum cores and IRAS object. It is possible that both outflows originate from IRAS 27.

The axis of the NEB−SWR flow is not as well centered on IRAS 27 as the SER−NWB outflow. An order of magnitude calculation, similar to the analysis in Section (3.2.1), reveals the volume density of the environment, n_{H_2}, is less than the density required to redirect the outflow ($n_{cl} \sim 10^6$ cm^{-3}). The alignment of HH and ^{12}CO $(3-2)$ outflows prompted suggestions that IRAS 27 is a binary source with each component driving an outflow (Reipurth et al. 2004). If so, then following the same procedure as for IRAS 25, we estimate ~ 1 M$_\odot$ for the mass of the stellar object(s) associated with IRAS 27.

3.2.3. Outflow Analysis

Optical Depth, Excitation Temperature, & H$_2$ Column Density

Outflow characteristics and energetics analyses were carried out under assumptions of constant excitation throughout the mapped regions and Local Thermodynamic Equilibrium (LTE). With pointed observations toward IRAS 25 & 27 in ^{12}CO $(3-2)$, ^{13}CO $(3-2)$, and ^{12}CO $(1-0)$, measurements of optical depth and excitation temperature were made and H$_2$ column density was derived. Optical depth, τ, was found using ^{13}CO $(3-2)$ and ^{12}CO $(3-2)$ observations. Assuming ^{12}CO & ^{13}CO have comparable excitation temperatures due to their similarity in rotational energy level structures, the ratio of their optical depths is the abundance ratio, r_a (see Equation 4).

$$\frac{I_{^{12}CO}}{I_{^{13}CO}} = \frac{1 - e^{-r_a \tau_{32}^{^{13}CO}}}{1 - e^{-\tau_{32}^{^{13}CO}}} \tag{4}$$

Optical depth of the ^{13}CO was determined by making a ratio of the integrated intensities of the ^{12}CO & ^{13}CO spectra, $I_{^{12}CO}$ and $I_{^{13}CO}$, respectively. An abundance ratio $r_a = 60$ for ^{12}CO to ^{13}CO was used (Kulesa 2003), Equation 4 was solved numerically.

After convolving ^{12}CO $(3-2)$ and ^{12}CO $(1-0)$ data sets to the same beamsize ($\sim 1'$) and converting each temperature scale into T_{mb} as described in Section (2.2), line ratios of the spectra were used to determine T_{ex} (Walker 1991). In this analysis, the ^{12}CO $(3-2)$ and ^{12}CO $(1-0)$ emission was assumed to originate from the same volume and since our data sets were convolved to the same beamsize, the emission filling factors were the same. With this method, values of 20 K and 30 K were found for T_{ex} toward IRAS 25 and 27, respectively.

With estimates of optical depth and excitation temperature, the ^{13}CO $(3-2)$ column density was determined with the following expression (Groppi et al. 2004; Walker et al. 1988):

$$N_{\nu, thin} = T_{ex} \tau \Delta v \; \frac{6k}{8\pi^3 \nu \mu^2} \; \frac{2l+1}{2u+1} \; \frac{e^{lh\nu/(2kT_{ex})}}{(1 - e^{-h\nu/(kT_{ex})})} \tag{5}$$

In the above equation, l is the lower rotational state, u describes the upper state, k and h are respectively Boltzmann's and Planck's constants, ν is the $^{13}CO\,(3-2)$ frequency, Δv is the velocity interval over which the column density was calculated, and μ is the molecular dipole moment expressed in esu. The above expression describes how to calculate the column density toward a position where the values of τ & T_{ex} are known. Pointed $^{13}CO\,(3-2)$ observations were made toward individual IRAS sources, though $^{13}CO\,(3-2)$ data were not available over the regions mapped in $^{12}CO\,(3-2)$. For this reason, excitation temperature, optical depth, and column density values were obtained at the positions of the IRAS sources, although calculating this information directly over the mapped regions was not possible. Table 7 presents LTE properties of IRAS 25 and 27 calculated for red and blue line wings.

In order to obtain column density information and ultimately mass and energetics information for outflows NGC 2264 O & H an emission-weighted area technique was used (Lada 1985). The analysis assumed the observed intensity ratio of $^{12}CO\,(3-2)$ and $^{13}CO\,(3-2)$ emission at the positions of the IRAS sources was constant over the regions mapped in $^{12}CO\,(3-2)$. It was also assumed that T_{ex} obtained at the positions of IRAS sources was constant over the mapped areas. The intensities of the $^{12}CO\,(3-2)$ emission measured toward the IRAS sources, where $N_{\nu,thin}$ was calculated, were compared with $^{12}CO\,(3-2)$ emission over the entire maps and used to weight the contribution of individual map positions to the total emission weighted area of the outflow, A_{weight}. This procedure is described in Equation 6, where A_{beam} is the area of the telescope beam at $345\,GHz$, $I_{x,y}$ is the $^{12}CO\,(3-2)$ intensity at any map position, and $I_{IRAS\ 25/27}$ is the $^{12}CO\,(3-2)$ intensity at IRAS 25 or 27, depending on the map examined.

$$A_{weight} = \sum_{x,y}^{map} A_{beam}\left(\frac{I_{x,y}}{I_{IRAS\ 25/27}}\right) \tag{6}$$

$$M_{OF} = \frac{N_{\nu\ thin}}{r_a r_{H_2}}\, A_{weight}\, m_{H_2}\, f_{thin} \tag{7}$$

Using the emission-weighted area method, the gas mass associated with the outflow was obtained using Equation 7. In this equation, m_{H_2} is the molecular hydrogen mass and f_{thin} is the $^{13}CO\,(3-2)$ gas filling factor. The filling factor was calculated using T_{ex}, the integrated intensity and optical depth of the $^{13}CO\,(3-2)$, and assuming LTE conditions. Filling factors obtained toward IRAS sources appear in Table 7. Since $^{13}CO\,(3-2)$ measurements were made toward single positions, f_{thin} was assumed to be constant over the maps. In Equation 7, r_a is the $^{12}CO/^{13}CO$ abundance ratio. We adopted $r_a = 60$ in agreement with the work of Kulesa (2003). The CO/H_2 abundance, $r_{H_2} = 1 \times 10^{-4}$, is representative of the ISM and

many nearby molecular clouds. Results of our mass analysis for the red and blue NGC 2264 O & H outflow lobes are provided in Table 8.

Outflow Energetics

With outflow masses, we were able to derive other physical properties of NGC 2264 O & H, including momentum ($P_{OF} = M_{OF}\ v_{max}$), kinetic energy ($E_{OF} = 1/2\ M_{OF}\ v^2_{max}$), mechanical luminosity ($L_{OF} = E_{OF}/t_{dyn}$), mass outflow rate ($\dot{M}_{OF} = M_{OF}/t_{dyn}$), and force ($\dot{P}_{OF} = P_{OF}/t_{dyn}$). In this analysis, $t_{dyn} = l_{wing}/v_{max}$ is the outflow dynamical age, l_{wing} is the outflow lobe physical extent measured from emission half-power contours, and v_{max} is the characteristic velocity of the outflowing material. LTE outflow energetics depend largely upon the choice of v_{max} which is subject to uncertainty due to projection effects of the outflow with respect to the line of sight. Determining a characteristic velocity representative of the bulk of the outflowing gas is therefore difficult. For this reason, lower and upper limits of the outflow energetics were determined using outer line wings of ^{13}CO $(3 - 2)$ (LV RW & LV BW) and ^{12}CO $(3 - 2)$ (F RW & F BW) for v_{max}. The results of these calculations appear in Table 8.

These energetics results are largely consistent with those of Margulis, Lada, & Snell (1988). Upper limit kinetic energy, momenta, and mechanical luminosities of the outflows are comparable to those typically associated with young high mass protostars, possessing $L_{FIR} = 10^2 - 10^5$ $L_{\odot}$ and $M_{OF} =$ tens of $M_{\odot}$ (Zhang et al. 2005). Since neither IRAS 25 nor 27 is believed to be a high mass star forming object, these results are consistant with the interpretation that the outflows arise from multiple objects.

4. Analysis & Discussion

4.1. Velocity Centroid Analysis

In order to explore the effect the NGC 2264 O & H molecular outflows have on the cloud environment, we constructed velocity centroid maps of the ^{12}CO $(3 - 2)$ gas. The velocity centroid is the value that equally divides the integrated intensity of a line profile. For this analysis, the velocity centroid was computed over the line core excluding emission in the wings (see Table 6). A map of velocity centroid as a function of position was generated for NGC 2264 O & H (see Figure 6 a and b). The centroid velocity values have been represented with labeled, thin contours. Half power contours of the red and blue wing ^{12}CO $(3 - 2)$ emission are depicted with thick solid and dashed lines, respectively. There is

a small gradient in velocity centroid values in each map, $\Delta v_{cent} = (7.65 - 6.6)$ km s$^{-1} \approx 1.1$ km s^{-1} and $\Delta v_{cent} = (8.35 - 7.4)$ km s$^{-1} \approx 1$ km s^{-1} for NGC 2264 O & H, respectively. There is no noticeable sign of rotation perpendicular to outflow axes to suggest the signature of an accretion disk. The centroid velocity gradients extend from the northeast corner of the plots to the southwest, roughly following the orientations of the outflow lobes. This suggests that NGC 2264 O & H outflows may dominate the energetics of their surroundings.

In order to illustrate this quantitatively, the force of bulk motions of cloud material was calculated and compared with the force of the molecular outflow, $\dot{P}_{OF}$. For this analysis, the mass of the cloud was computed over the line core for each ^{12}CO $(3-2)$ map, M_c, using the emission weighted area approach described in Section (3.2.3). This mass calculation assumes the ^{13}CO $(3-2)$ emission is optically thin over the line core. In order to assess the impact this might have on the analysis, the ^{13}CO $(3-2)$ optical depth was examined as a function of velocity toward the position of the IRAS sources, where direct calculations of optical depth and column density were made. For IRAS 25, the ^{13}CO $(3-2)$ emission is marginally thick in the line core, with optical depth $\sim 1-1.1$. The mass associated with line core velocities, and therefore the corresponding force calculations, should serve as a lower limits for NGC 2264 O. Over the line core region, the ^{13}CO $(3-2)$ emission toward IRAS 27 is thin, with optical depth values $\sim 0.3 - 0.35$, so the mass associated with the line core, and therefore the corresponding force calculations, are most likely valid.

Calculations of the force of bulk cloud motions were made using $\dot{P}_c = M_c \Delta v_{cent}/\tau_{dyn}$, where M_c is the mass in the line core region, Δv_{cent} is the observed centroid velocity gradient along the outflow axis, and τ_{dyn} is the dynamical age of the outflow. Using dynamical ages of the red and blue outflow lobes resulted in $\dot{P}_c = 6.6 - 11 \times 10^{-4} \, \mathrm{M}_\odot \, \mathrm{yr}^{-1}$ km s^{-1} for NGC 2264 O. This is more than ~ 5 times smaller than the force of the outflowing material, $\dot{P}_{OF} = 60 \times 10^{-4} \, \mathrm{M}_\odot \, \mathrm{yr}^{-1}$ km s^{-1}, obtained by summing the contributions of the red and blue wings shown in Table 8. These comparisons were also made for energetics and dynamical ages obtained using the ^{13}CO $(3-2)$ line wings to guide the analysis. Values of $\dot{P}_c = 3.7 - 6.2 \times 10^{-4} \, \mathrm{M}_\odot \, \mathrm{yr}^{-1}$ km s^{-1} were obtained for NGC 2264 O and are ~ 3 times smaller than $\dot{P}_{OF} = 18 \times 10^{-4} \, \mathrm{M}_\odot \, \mathrm{yr}^{-1}$ km s^{-1}. Overall, the values of $\dot{P}_c$ and $\dot{P}_{OF}$ are similar within factors of a few, indicating that the NGC 2264 O outflow has enough force to drive the bulk motions of the cloud material.

Performing a similar analysis for NGC 2264 H results in $\dot{P}_c = 3.7 - 7.3 \times 10^{-4} \, \mathrm{M}_\odot \, \mathrm{yr}^{-1}$ km s^{-1}. Compared with the force of the outflow, $\dot{P}_{OF} = 18 \times 10^{-4} \, \mathrm{M}_\odot \, \mathrm{yr}^{-1}$ km s^{-1}, $\dot{P}_c$ is several times smaller. Calculations made using line wings of the ^{13}CO $(3-2)$ emission for the outflow ages and energetics, find values of $\dot{P}_c = 2.1 - 2.2 \times 10^{-4} \, \mathrm{M}_\odot \, \mathrm{yr}^{-1}$ km s^{-1}, similar to the force of the outflow, $\dot{P}_{OF} = 2.4 \times 10^{-4} \, \mathrm{M}_\odot \, \mathrm{yr}^{-1}$ km s^{-1}. Values of $\dot{P}_c$ and $\dot{P}_{OF}$ are

within an order of magnitude, similar to NGC 2264 O. Again it appears that the outflow force is capable of driving bulk motions in the cloud.

4.2. Energetics Comparison

4.2.1. Turbulent Energy

The turbulent energy contributed to the cloud by the NGC 2264 O & H outflows, E_{turb}, was estimated using our $^{12}CO\,(3-2)$ data (observations of an optically thin species, such as $C^{18}O$, were not available). The estimate was made by comparing average FWHM velocity values at outflow wing emission peaks, $\Delta v(\text{on OF})$, to ambient cloud regions away from the outflow, $\Delta v(\text{Ambient})$. In all regions, the line wings were excluded from the Gaussian fit. Since the $^{12}CO\,(3-2)$ is optically thick, opacity broadening due to saturation effects should be considered (Phillips et al. 1979). Compared to an optically thin species, saturation is expected to broaden the FWHM of the ^{12}CO lines by factors of 2.6 and 2.2 toward IRAS 25 and 27, respectively. Normalizing our measured FWHM values by these factors and assuming that the ^{12}CO opacity is to first order constant over the mapped regions, we derive values of $\Delta v(\text{on OF}) = 0.81$ km s^{-1} and $\Delta v(\text{Ambient}) = 0.54$ km s^{-1} for $^{12}CO\,(3-2)$ emission surrounding IRAS 25. Normalized FWHM values of $\Delta v(\text{on OF}) = 0.86$ km s^{-1} and $\Delta v(\text{Ambient}) = 0.45$ km s^{-1} were obtained for IRAS 27.

FWHM velocity values measured toward peak outflow emission probe many cloud characteristics including turbulent velocity structures (v_{turb}), thermal broadening (kT/m), and potentially components due to cloud magnetic field (v_B): $\Delta v(\text{on OF}) = (v_{turb}^2 + kT/m + v_B^2)^{1/2}$. The turbulence associated with the FWHM velocity of the outflowing gas, v_{turb}, has two components. These are general cloud turbulence, $v_{turb\ cloud}$, present both toward and away from the outflow, and turbulence due to the outflow itself, $v_{turb\ OF}$. These components combine quadratically, $v_{turb}^2 = v_{turb\ cloud}^2 + v_{turb\ OF}^2$. The FWHM velocity measured toward ambient cloud regions away from outflow emission is $\Delta v(\text{Ambient}) = (v_{turb\ cloud}^2 + v_B^2 + kT/m)^{1/2}$. Combining these equations and correcting for opacity broadening effects, the turbulent velocity due to outflow motions, $v_{turb\ OF}$, was obtained from FWHM velocity measurements: $v_{turb\ OF}^2 = [\Delta v(\text{on OF})]^2 - [\Delta v(\text{Ambient})]^2$. The turbulent energy contributed to the cloud by the molecular outflow was found using $E_{turb} = 1/2\ M_{OF}\ v_{turb\ OF}^2$ where M_{OF} is the total outflow mass, obtained by summing contributions of red and blue outflow lobes (see Table 8). For regions surrounding IRAS 25 and 27, we found $E_{turb} = 0.75\,M_\odot$ km^2 s^{-2} and $0.37\,M_\odot$ km^2 s^{-2}, respectively.

The coupling efficiency of outflow energy to the ambient cloud was estimated by com-

paring the turbulent cloud energy contributed by outflows, E_{turb}, and outflow kinetic energy, E_{OF} (see Table 9). Values of E_{OF} are orders of magnitude larger than E_{turb}, resulting in coupling efficiencies of $\leq 0.5\%$ in the regions surrounding IRAS 25 and 27. The low coupling efficiency of molecular outflow energy to the surrounding environment together with the results of our centroid velocity analysis suggests that most of the outflows' energy is directed along the flow axis and deposited in the intercloud medium leaving adjacent regions of the parent cloud largely undisturbed.

4.2.2. Gravitational Binding Energy

Clump gravitational binding energy, E_{GC}, was obtained using results of the continuum analysis (Table 5) and the expression for gravitational potential energy of a uniform gravitating sphere of constant density, $E_{GC} = 3/5 \, (G \, M_{H_2}^2/R)$. Here G is the gravitational constant, M_{H_2} is the molecular mass, and R is the sphere radius used to compute M_{H_2}. For IRAS 25, the average clump radius is $\sim 34''$ and substitution yields $E_{GC} = 640 \mathrm{M}_\odot \, \mathrm{km^2 \, s^{-2}}$.

The continuum image of the region surrounding IRAS 27 contains three sources, 27 S1, 27 S2, and 27 S3. Core masses, M_{H_2}, derived from $870 \, \mu\mathrm{m}$ flux measurements were used to individually determine contributions to E_{GC} for the three sources. Since the core masses, M_{H_2}, were derived from fluxes observed within $45''$ apertures, $R = 22.5''$ was used to obtain E_{GC} of individual cores. The results were summed to estimate the total clump gravitational potential energy: $E_{GC} = 5.5 \mathrm{M}_\odot \, \mathrm{km^2 \, s^{-2}}$. The result is included in Table 9 and is a lower limit to PE_{GC} since individual sources lie along a ridge of extended low-intensity $870 \, \mu\mathrm{m}$ emission. The mass associated with the low-level emission was not found since the FIR SED analysis did not apply.

Table 9 compares outflow kinetic energy, turbulent energy contributed to the cloud by outflows, and cloud clump potential energy for the regions surrounding IRAS 25 and 27. The molecular cloud appears to remain gravitationally bound, since turbulent energy injected into the cloud by outflows, E_{turb}, is much smaller than the cloud clump potential energy, E_{GC}. The low outflow energy coupling efficiency may explain why, even in the presence of multiple outflows, the cloud cores appear to maintain their overall integrity, with $E_{GC} \gg E_{turb}$. The dismantling effects the NGC 2264 O & H outflows are having on the molecular cloud appear to be largely localized to the portions of the clouds contained within opening angles of the outflow lobes.

5.   Summary

We have made $870\,\mu$m continuum measurements and ^{12}CO$\,(3-2)$, ^{13}CO$\,(3-2)$, and ^{12}CO$\,(1-0)$ observations of IRAS 25 & 27 in the northern cloud complex of NGC 2264 using the HHT and 12m telescopes. Continuum $870\,\mu$m OTF maps $(5'{\times}5')$ were made toward the sources IRAS 25 (IRAS 06382+1017) & 27 (IRAS 06381+1039) and several continuum cores were identified. SEDs were constructed for the cores and used to derive column densities, gas masses, FIR luminosities, and dust temperatures. A molecular line and energetics analysis of the outflows associated with NGC 2264 O & H was performed and multiple outflows were found within each region. In order to assess the impact star formation is having on the NGC 2264 cloud, the turbulent energy, outflow dynamical energy, and cloud clump gravitational potential energy were compared. The results are consistent with the interpretation that the cloud complexes are maintaining their overall integrity except along outflow axes where cloud material directly interacts with the outflows. The outflows deposit most of their energy outside of the molecular cloud, resulting in a weak $\leq 0.5\%$ coupling between outflow kinetic energy and cloud turbulent energy.

REFERENCES

Blitz, L. 1979, PhD thesis, Columbia Univ.

Bohlin, R. C., Savage, B. D. & Drake, J. F. 1979, ApJ, 224, 132.

Groppi, C. E., Kulesa, C., Walker, C. K., Martin, C. L. 2004, ApJ, 612, 946

Hildebrand, R. H. 1983, QJRAS, 24, 267.

Kulesa, C. 2003, PhD thesis, Univ. of Arizona

Lada, C. J. 1985, ARA&A, 23, 267.

Margulis, M. S., & Lada, C. J. 1985, ApJ, 299, 925.

Margulis, M. S., Lada, C. J., & Snell, R. L. 1988, ApJ, 333, 316.

Margulis, M. S., Lada, C. J., & Young, E. T. 1989, ApJ, 345, 906.

Ogura, K. 1995, ApJ, 450, L23.

Oliver, R. J., Masheder, M. R. W., & Thaddeus, P. 1996, A&A, 315, 578.

Phillips, T. G., Huggins, P. J., Wannier, P. G. & Scoville, N. Z. 1979, ApJ, 231, 720.

Piché, F., Howard, E. M., & Pipher, J. L. 1995, A&A, 275, 711.

Reipurth, B., Yu, Ka Chun, Moriarty-Schieven, G., Bally, J., Aspin, C., & Heathcote, S. 2004, AJ, 127, 1069.

Rodríguez, L. F. & Reipurth, B. 1998, RevMexAA, 34, 13.

Sandell, G. 1994, MNRAS, 271, 75.

Shu, F. H. 1977, ApJ, 214, 488.

Stahler, S. W., Shu, F. H., & Taam, R. 1980, ApJ, 241, 637.

Walker, C. E., 1990, PhD Thesis, Univ. of Arizona

Walker, C. K., Lada, C. J., Young, E. T., & Margulis, M. S., 1988, ApJ, 332, 335.

Walker, M. F., 1956, ApJS, 2, 365.

Walker, C. K., Adams, F. C., & Lada, C. J. 1990, ApJ, 349, 515.

Walsh, J. R., Ogura, K., & Reipurth, B. 1992, MNRAS, 257, 110.

Wolf-Chase, G. A., Moriarty-Schieven, G., Fich, M. & Barsony, M. 2003, MNRAS, 344, 809.

Wolf-Chase, G. A., Walker, C. K., & Lada, C. J. 1995, ApJ, 442, 197.

Zhang, Q., Hunter, T. R., Brand, J., Sridharan, T. K., Cesaroni, R., Molinari, S., Wang, J., & Kramer, M. 2005, ApJ, 625, 864.

Table 1.   Spectral Line Observations

Object	α_{1950}	δ_{1950}	Telescope	Spectral Line	Dates	Mode	Map Size ($''$)	Resolution (km s^{-1})	(kHz)	2σ RMS (K)	Beam Size ($''$)	(pc)
IRAS 25 (NGC 2264 O)	06:38:17.0	10:18:00.0	HHT	^{12}CO$(3-2)$	2004 Feb 25-27	OTF	300×300	0.886	1021	0.3	22	0.08
IRAS 25 (NGC 2264 O)	06:38:17.0	10:18:00.0	HHT	^{13}CO$(3-2)$	2004 Feb 25-27	APS	$\cdots$	0.927	1021	0.06	23	0.09
IRAS 25 (NGC 2264 O)	06:38:17.0	10:18:00.0	12m	^{12}CO$(1-0)$	2002 Apr 08-10	APS	$\cdots$	0.254	97.6	0.1	55	0.21
NGC 2264 H	06:38:16.8	10:39:45.0	HHT	^{12}CO$(3-2)$	2004 Feb 25-27	OTF	300×300	0.886	1021	0.22	22	0.08
IRAS 27	06:38:13.0	10:39:45.0	HHT	^{13}CO$(3-2)$	2004 Feb 25-27	APS	$\cdots$	0.927	1021	0.06	23	0.09
IRAS 27	06:38:13.0	10:39:45.0	12m	^{12}CO$(1-0)$	2002 Apr 08-10	APS	$\cdots$	0.254	97.6	1.2	55	0.21

Table 2.   870 μm Source Flux

Source	α_{1950}	δ_{1950}	45$''$ Aperture Flux (Jy)	3$'$ × 5$'$ Aperture Flux (Jy)
IRAS 25	06:38:17.0	10:18:00.0	2.60±0.52	8.29±1.66
25 S1	06:38:17.8	10:18:02.6	6.36±1.27	⋯
25 S2	06:38:19.2	10:17:47.7	5.99±1.20	⋯
IRAS 27 (27 S1)	06:38:13.0	10:39:45.0	3.81±0.64	22.38±4.48
27 S2	06:38:13.0	10:39:01.0	2.24±0.45	⋯
27 S3	06:38:15.9	10:38:22.5	1.96±0.39	⋯

Table 3.   Source Flux

Source	Wavelength (μm)	Flux (Jy)	σ RMS (Jy)	Aperture ($''$)	References
IRAS 25	870	8.29	1.66	180×300	1
	850	6.25	1.25	180×300	2
	450	21.9	4.38	180×300	2
	100	86.66	30.33	180×300	3
	60	43.45	8.69	90×285	3
	25	7.908	0.949	45×276	3
	12	1.283	0.192	45×270	3
IRAS 27 (27 S1)	1300	0.8	0.16	27.3	2
	870	3.81	0.76	45.0	1
	850	3.20	0.64	45.0	2
	450	31.8	6.36	45.0	2
	100	144.9	37.67	180×300	3
	60	53.66	11.81	90×285	3
	25	2.755	0.193	45×276	3
	12	0.25	0.001	45×270	3
27 S2	1300	0.7	0.14	27.3	2
	870	2.24	0.45	45.0	1
	850	1.87	0.37	45.0	2
	450	12.1	2.42	45.0	2
	100	144.9	37.67	180×300	3
	60	53.66	11.81	90×285	3
	25	2.755	0.193	45×276	3
	12	0.25	0.001	45×270	3
27 S3	870	1.96	0.39	45.0	1
	850	1.72	0.34	45.0	2
	450	12.9	2.58	45.0	2
	100	144.9	37.67	180×300	3
	60	53.66	11.81	90×285	3
	25	2.755	0.193	45×276	3
	12	0.25	0.001	45×270	3

Note. — References: (1) This work. (2) Wolf-Chase et al. (2003) (3) IRAS PSC

Table 4. Parameters of FIR SED Model Fits

Source	T (K)	τ_{870}	β	Ω_m	Ω_s	f_d	L_{FIR} ($L_\odot$)
IRAS 25	10	1.3×10^{-2}	1.4	1.2×10^{-8}	2.4×10^{-9}	21×10^{-2}	88
	40	1.5×10^{-3}	1.4	1.2×10^{-8}	2.0×10^{-10}	1.7×10^{-2}	88
IRAS 27 (27 S1)	30	2.7×10^{-3}	1.4	1.7×10^{-8}	9.3×10^{-10}	5.3×10^{-2}	120
27 S2	36	1.3×10^{-3}	1.2	1.7×10^{-8}	3.2×10^{-10}	1.9×10^{-2}	92
27 S3	33	1.2×10^{-3}	1.4	1.7×10^{-8}	5.1×10^{-10}	2.9×10^{-2}	100

Table 5. Core Properties

Source	M_{H_2} ($M_\odot$)	N_{H_2} (cm^{-2})	n_{H_2} (cm^{-3})	A_v
IRAS 25	140	3.0×10^{23}	3.0×10^{5}	330
IRAS 27 (27 S1)	12	7.0×10^{22}	8.8×10^{4}	77
27 S2	3.4	1.9×10^{22}	2.5×10^{4}	21
27 S3	5.5	3.2×10^{22}	4.0×10^{4}	35

Table 6. CO$(3-2)$ Line Wings

Source	F BW (km s^{-1})	HV BW (km s^{-1})	LV BW (km s^{-1})	Line Core (km s^{-1})	LV RW (km s^{-1})	HV RW (km s^{-1})	F RW (km s^{-1})
IRAS 25	-10.5, 5.6	-10.5, -2.5	-2.5, 5.6	5.6, 8.8	8.8, 19.0	19.0, 27.5	8.8, 27.5
IRAS 27	-20.0, 6.7	-20.0, 0.0	0.0, 6.7	6.7, 9.8	9.8, 20.0	20.0, 28.5	9.8, 28.5

Table 7. LTE Outflow Analysis Properties

Source	Line Wing	T_{ex} (K)	τ_{32}^{13CO}	$N_{\nu, thin}$ ($\times 10^{15}$ cm^{-2})	N_{H_2} ($\times 10^{21}$ cm^{-2})	f_{thin}
IRAS 25	F RW	20	0.16	14	8.6	0.17
IRAS 25	F BW	20	0.28	22	13	0.10
IRAS 27	F RW	30	0.10	14	8.5	0.04
IRAS 27	F BW	30	0.03	6.6	3.9	0.06

Table 8.   NGC 2264 ^{12}CO$(3-2)$ Outflow Energetics

Outflow	v_{max} (km s^{-1})	M_{OF} (M$_\odot$)	P_{OF} (M$_\odot$ km s^{-1})	E_{OF} ($\times 10^2$ M$_\odot$ km^2 s^{-2})	L_{OF} (L$_\odot$)	$\dot{M}_{OF}$ ($\times 10^{-5}$ M$_\odot$ yr^{-1})	t_{dyn} ($\times 10^4$ yr)	$\dot{P}_{OF}$ ($\times 10^{-4}$ M$_\odot$ yr^{-1} km s^{-1})
O (LV RW)	11	1.5	16	0.9	0.81	8.1	1.8	8.1
O (LV BW)	10.5	2.9	31	1.6	0.89	9.8	3.0	10
O (F RW)	19.5	1.5	29	2.8	4.5	14	1.0	28
O (F BW)	18.5	2.9	54	5.0	4.9	17	1.7	32
H (LV RW)	12	0.59	7.1	0.43	0.13	1.1	5.4	1.3
H (LV BW)	8.0	0.79	6.3	0.25	0.07	1.4	5.7	1.1
H (F RW)	20.5	0.59	12	1.2	0.65	1.9	3.2	3.8
H (F BW)	28	0.79	22	3.1	3.1	4.9	1.6	14

Note. — Nomenclature: O = NGC 2264 O and H = NGC 2264 H

Table 9.   Cloud Core Energetics

Source	M_{H_2} (M$_\odot$)	M_{OF} (M$_\odot$)	E_{GC} (M$_\odot$ km^2 s^{-2})	E_{OF} (M$_\odot$ km^2 s^{-2})	E_{turb} (M$_\odot$ km^2 s^{-2})	Comparison
IRAS 25	140	4.1	640	$430 - 780$	0.75	$E_{GC} \sim 850\, E_{turb}$
IRAS 27	21	1.4	5.5	$68 - 250$	0.37	$E_{GC} \sim 15\, E_{turb}$

Note. — E_{OF} values were determined using ^{13}CO $(3-2)$ and ^{12}CO $(3-2)$ line wings, respectively.
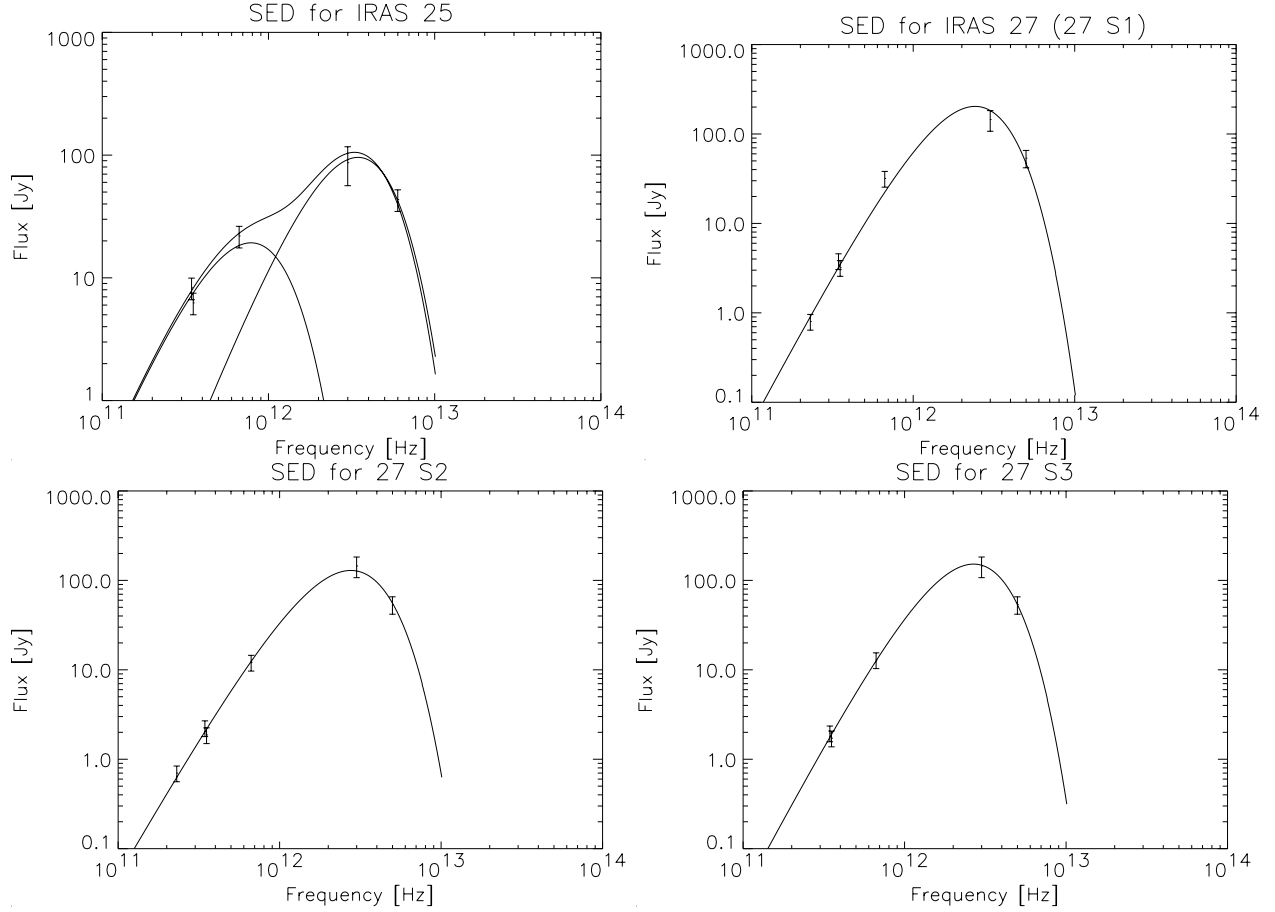
Fig. 1.— FIR SEDs for sources IRAS 25, IRAS 27 (27 S1), 27 S3, & 27 S2 (clockwise from upper left). From the shortest wavelength, fluxes included are IRAS 60 μm and 100 μm data, 450 μm and 850 μm SCUBA measurements, 870 μm HHT data from this study, and where available (IRAS 27 and 27 S2), 1300 μm fluxes. For IRAS 25, a two component BB function was fit to this SED. All other sources are well described by single temperature functions.
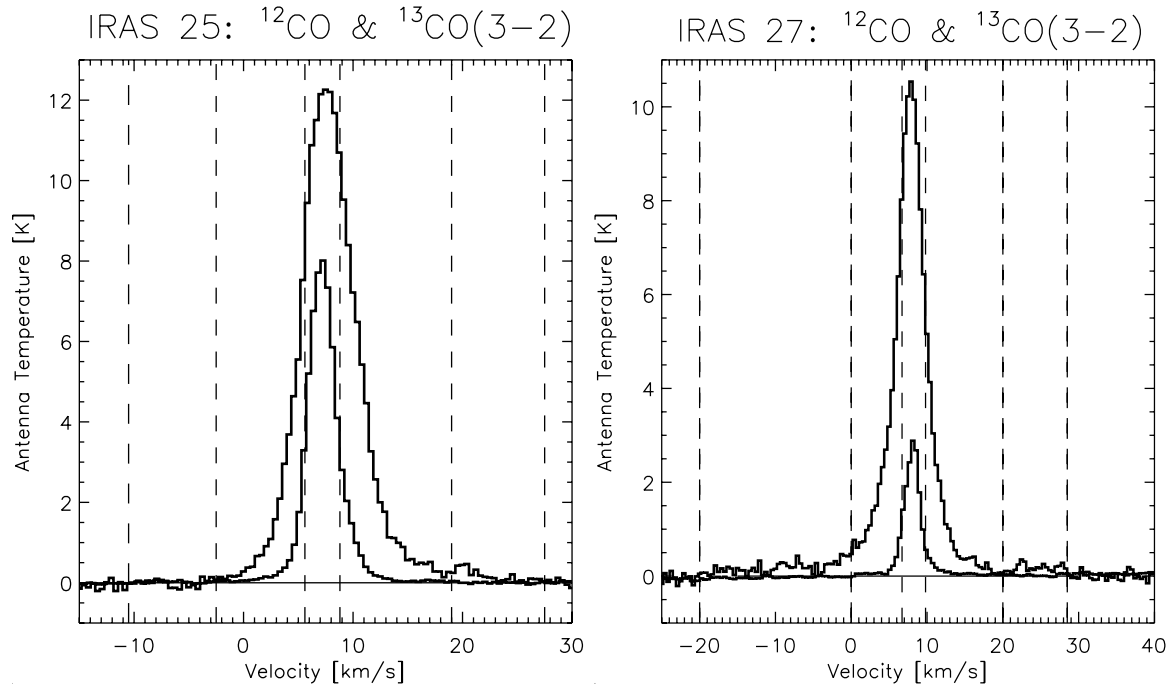
Fig. 2.— ^{12}CO & ^{13}CO $(3-2)$ overlayed spectra of IRAS 25 and 27. Vertical lines show LV and HV red and blue wings and line core (see Table 6).
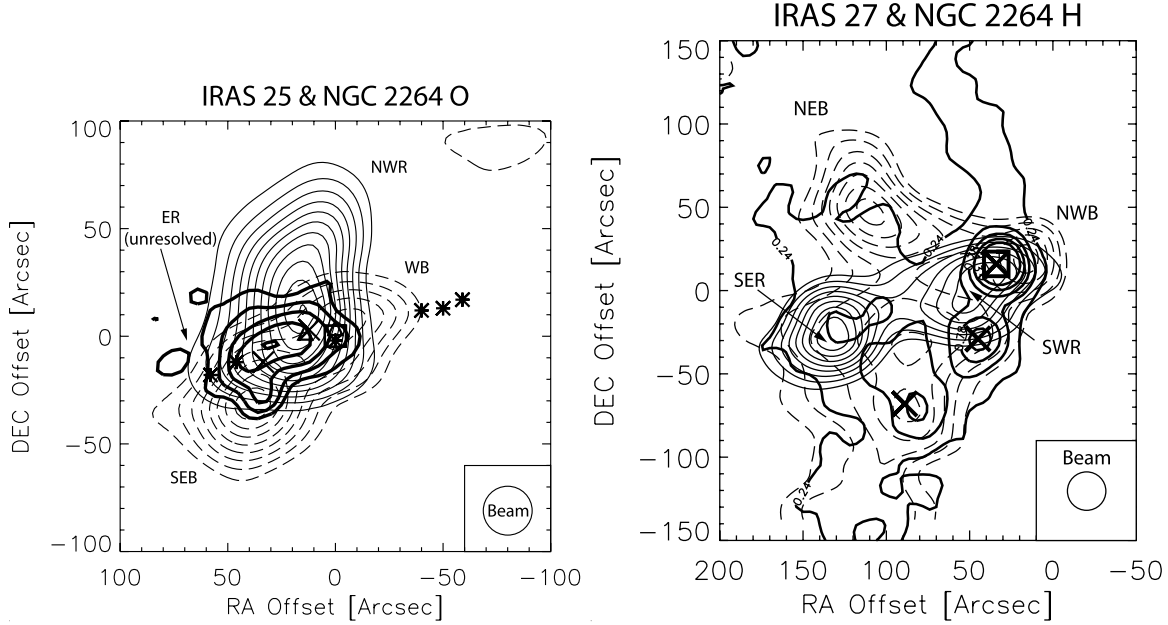
Fig. 3.— Contours of red (solid) and blue (dashed) $^{12}CO\,(3-2)$ outflow emission associated with NGC 2264 O & H overlayed on $870\,\mu m$ continuum maps (thick solid lines). Locations of sources within each region are shown, including IRAS 25 & 27 (squares), submillimeter continuum objects ("X"), HH 124 emission knots (asterisks), and VLA sources (triangles). Continuum $870\,\mu m$ contours begin at $2\sigma = 0.38\,Jy$ and $3\sigma = 0.16\,Jy$ for IRAS 25 & 27, respectively, increasing in steps of $0.29\,K$ & $0.27\,K$ toward emission peaks, $1.85\,Jy$ and $2.25\,Jy$. F RW contours begin at $6.6\,K\,km\,s^{-1}$ for NGC 2264 O & H increasing in $2.6\,K\,km\,s^{-1}$ steps toward emission peaks, $36\,K\,km\,s^{-1}$ and $31\,K\,km\,s^{-1}$, respectively. F BW contours start at $6.3\,K\,km\,s^{-1}$ and $6.8\,K\,km\,s^{-1}$ for NGC 2264 O & H, respectively, and increase by $1.3\,K\,km\,s^{-1}$ and $2.6\,K\,km\,s^{-1}$. Peak F BW emission is $17\,K\,km\,s^{-1}$ and $32\,K\,km\,s^{-1}$ for NGC 2264 O & H, respectively.
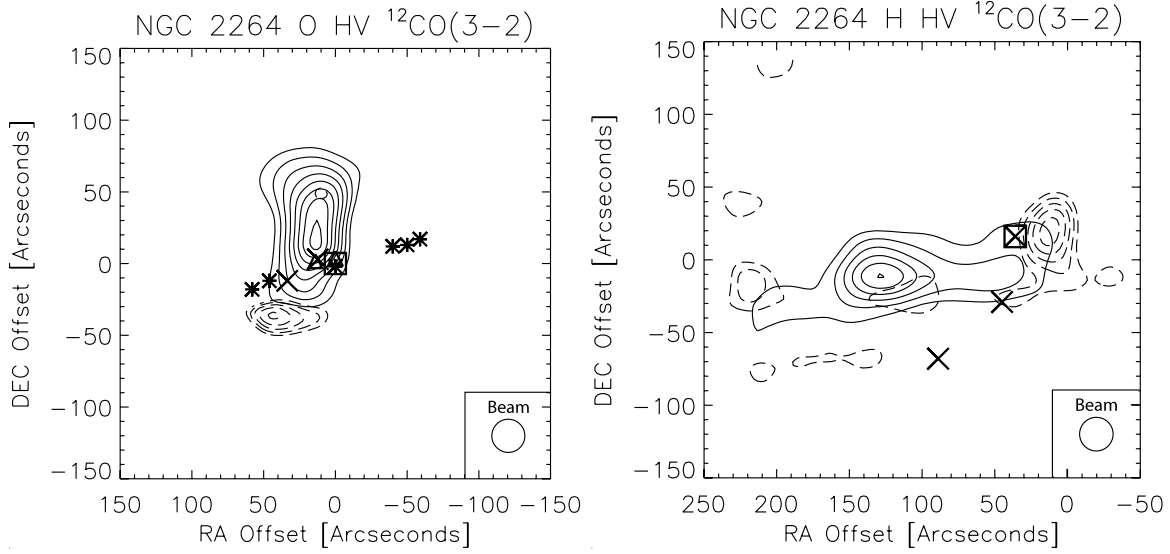
Fig. 4.— Contours of the HV red (solid) & blue (dashed) ^{12}CO $(3-2)$ emission (see Table 6) associated with NGC 2264 O & H. HV blue contours begin at $2\,\sigma = 1.6$ K km s^{-1} and $2\,\sigma = 1.5$ K km s^{-1}, increasing in steps of 0.15 K km s^{-1} and 0.7 K km s^{-1} for NGC 2264 O & H, respectively. Contours of HV red emission begin at $2\,\sigma = 1.8$ K km s^{-1} and $2\,\sigma = 1.0$ K km s^{-1}, increasing by 0.8 K km s^{-1} and 1.0 K km s^{-1}. HV emission peaks at 2.2 K km s^{-1} and 5.4 K km s^{-1} (blue) and 8.2 K km s^{-1} and 7.0 K km s^{-1} (red) for NGC 2264 O & H, respectively.
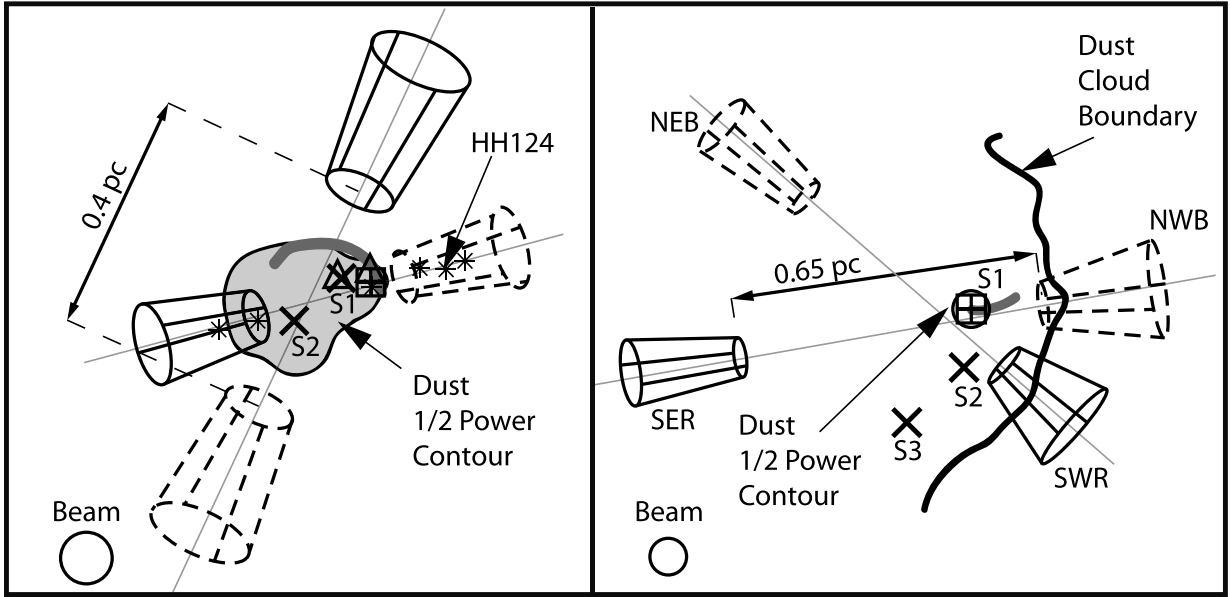
Fig. 5.— Model of the ^{12}CO $(3-2)$ outflows surrounding IRAS 25 & 27 (left to right). The red (solid) & blue (dashed) lobes of the outflows and their approximate positions with respect to half power $870\,\mu$m continuum contours are indicated. Two molecular outflows are present in each region. The sizes, orientations, and locations of IR reflection nebulae associated with IRAS 25 & 27 are indicated with solid arcs.
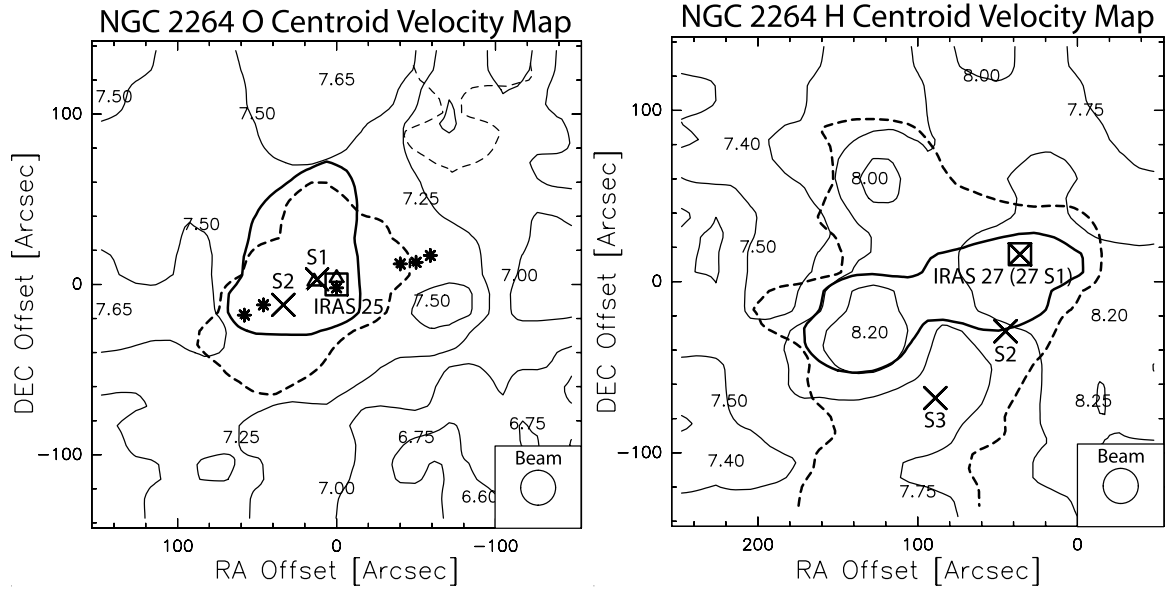
Fig. 6.— Velocity centroid maps of ^{12}CO $(3-2)$ line core emission associated with NGC 2264 O & H. Velocity centroid contours (thin solid lines) are shown and labeled (km s^{-1}). Half power contours of red and blue outflow emission are illustrated with thick solid and dashed contours, respectively.